

## MATERIALS SCIENCE

## Graphene reinforced carbon fibers

Zan Gao<sup>1</sup>, Jiadeng Zhu<sup>1</sup>, Siavash Rajabpour<sup>2</sup>, Kaushik Joshi<sup>3</sup>, Małgorzata Kowalik<sup>4</sup>, Brendan Croom<sup>1</sup>, Yosyp Schwab<sup>1</sup>, Liwen Zhang<sup>1</sup>, Clifton Bumgardner<sup>1</sup>, Kenneth R. Brown<sup>1</sup>, Diana Burden<sup>1</sup>, James William Klett<sup>5</sup>, Adri C. T. van Duin<sup>2,4\*</sup>, Leonid V. Zhigilei<sup>3\*</sup>, Xiaodong Li<sup>1\*</sup>

The superlative strength-to-weight ratio of carbon fibers (CFs) can substantially reduce vehicle weight and improve energy efficiency. However, most CFs are derived from costly polyacrylonitrile (PAN), which limits their widespread adoption in the automotive industry. Extensive efforts to produce CFs from low cost, alternative precursor materials have failed to yield a commercially viable product. Here, we revisit PAN to study its conversion chemistry and microstructure evolution, which might provide clues for the design of low-cost CFs. We demonstrate that a small amount of graphene can minimize porosity/defects and reinforce PAN-based CFs. Our experimental results show that 0.075 weight % graphene-reinforced PAN/graphene composite CFs exhibits 225% increase in strength and 184% enhancement in Young's modulus compared to PAN CFs. Atomistic ReaxFF and large-scale molecular dynamics simulations jointly elucidate the ability of graphene to modify the microstructure by promoting favorable edge chemistry and polymer chain alignment.

## INTRODUCTION

Carbon fibers (CFs), composed of 92 to 100 weight % (wt %) anisotropic carbon, are typically manufactured through a series of controlled thermal treatments of precursor polymer fibers (1). The unique properties of CFs, such as their high tensile strength, low density, high modulus, and excellent creep and chemical resistance, have made them the leading reinforcing materials for lightweight composite applications (2). Since its first commercialization in the 1960s, the usage of CFs is still limited to high-end applications, such as aerospace, military, sporting goods, and some other specialized industries, due to their high cost (3). However, increasing pressure to reduce vehicle emissions and improve fuel efficiency has amplified the desire to use low-cost, lightweight CF-reinforced composites in the automotive industry. CF-reinforced composites are forecasted to play a significant role in improving the energy efficiency of all vehicles by replacing traditional metal components. Driven by this vision, many efforts have been devoted to reducing the material and processing costs of CFs and designing CF-reinforced composite materials with excellent mechanical properties through optimized interfacial control (4–6). Currently, more than 90% of the CF market is dominated by expensive polyacrylonitrile (PAN) precursors because of their high carbon yield (up to 56%) and wide processing tolerances (7). However, more than 50% of the cost of traditional PAN-derived CFs is attributed to the PAN precursor alone. The high cost of PAN motivates the search for low-cost alternative precursors to enable new uses of CFs. To date, cheap and renewable raw materials, such as pitch, cellulose, lignin, rayon, and some other synthetic and semisynthetic polymers, have been explored to replace PAN and lower the cost of CFs (8–11). Unfortunately, the poor mechanical properties of CFs derived from these low-cost precursors

restrict their usage. Therefore, a robust approach to filter for low-cost CFs should be a multitier strategy of (i) revisiting the successful PAN precursor and its processing methods; (ii) understanding the fundamental principles underlying the conversion chemistry, microstructure evolution, and structure-processing-property relationship; and (iii) investigating mechanisms to enhance the mechanical properties of low-cost CFs.

PAN-based CFs are typically manufactured by a wet or dry-jet spinning of polymer filaments that are then converted to CFs by a series of thermal treatments, including thermal stabilization, carbonization, and graphitization (12). Specifically, PAN precursor fibers are first oxidized at temperatures ranging between 200° and 300°C in atmospheric air, which enables the formation of a more stable, infusible N-containing ladder structures that are necessary for the subsequent high-temperature carbonization. Next, the stabilized fibers are carbonized between 1200° and 1600°C, which eliminates noncarbon atoms to form a turbostratic carbon structure. Last, the fibers are graphitized at temperatures above 2100°C to convert the turbostratic structure into a more ordered structure characterized by the presence of graphitic domains (13). The performance of PAN-based CFs relies on the quality of the precursor fibers and the delicate thermal processing steps. It has been widely recognized that the higher the degree of molecular orientation of the original PAN precursor fiber, the better the mechanical properties of the final CFs (14). However, the difficulty of quality control for PAN precursor fibers and the complexity of optimizing the thermal treatments has motivated research efforts to develop cost-effective and robust spinning and processing methods to prepare CFs, such as plasma or electron beam irradiation-assisted stabilization, and boron-assisted graphitization (15–18).

Currently, wet spinning is the preferred method of producing PAN-based precursor fibers. In the wet spinning process, spinning dope is extruded through a spinneret into a coagulation bath where the solvent can be diffused out, while the PAN polymer is solidified into precursor fibers (19). The physical, chemical, and mechanical properties of the precursor fibers are influenced by several processing parameters, such as the structure and content of the copolymer, molecular weight of the precursor polymer, polydispersity index, solvent and solid content of the spinning dope, solvent/nonsolvent ratio, temperature of coagulation bath, and the stretching and draw

<sup>1</sup>Department of Mechanical and Aerospace Engineering, University of Virginia, 122 Engineer's Way, Charlottesville, VA 22904, USA. <sup>2</sup>Department of Chemical Engineering, The Pennsylvania State University, University Park, PA 16802, USA. <sup>3</sup>Department of Materials Science and Engineering, University of Virginia, 395 McCormick Road, Charlottesville, VA 22904-4745, USA. <sup>4</sup>Department of Mechanical Engineering, The Pennsylvania State University, University Park, PA 16802, USA. <sup>5</sup>Oak Ridge National Laboratory, Oak Ridge, TN 37830, USA.

\*Corresponding author. Email: acv13@psu.edu (A.C.T.v.D.); lz2n@virginia.edu (L.V.Z.); xl3p@virginia.edu (X.L.)

ratio during the spinning and post-washing processes (20–23). The spinning and subsequent stabilization processes determine the alignment, orientation, and crystallization of the polymer chain and microstructure of the precursor fibers, which has a great effect on the mechanical properties of the final CFs. For instance, lowering the bath temperature can limit the occurrence and size of large pores and voids (22). Stretching in the bath and post-drawing during the stabilization process can increase the molecular alignment of the polymer chains (23). In addition to optimizing the spinning dope and coagulation parameters, adding carbon nanotubes (CNTs) into the polymer matrix has been regarded as a promising technique to improve the mechanical properties of the composite fiber; CNTs can serve as both the template for the alignment and orientation of polymer chain and the nucleating agent for the polymer crystallization (24–26). For example, Chae *et al.* (27) reported that the addition of 1.0 wt % carbon nanotubes could enhance the CF modulus by 49% and strength by 64%. The addition of CNTs also lowered the carbonization temperature, which can significantly reduce the energy consumption during CF manufacturing (28). Graphene, a single-layered two-dimensional (2D) carbon allotrope, demonstrates superior properties to CNTs, such as larger surface area, superior electron mobility, higher tensile strength, and Young's modulus, which make it ideal for various applications, such as energy storage, metamaterials, and reinforced composite materials (29–32). Recently, graphene oxide (GO) liquid crystal, a derivative of graphene, was evaluated for the fabrication of CFs using various approaches, such as wet spinning, dry spinning, dry-jet wet spinning, electrophoretic self-assembly, and film shrinkage and twisting methods (33). However, the GO-derived CFs exhibited subpar tensile strength because of their poor intrinsic alignment and crystallinity (34–36).

On the basis of the superior properties of graphene, pristine graphene may be a better additive than CNTs and GO for the PAN-based CFs. Recent reports demonstrate the potential of the usage of graphene as a structure-directing agent to tune the orientation and graphitization of polymers (37, 38). In this work, a small amount of shear-exfoliated pristine graphene (ranging from 0.01 to 1.0 wt %) was first introduced into a PAN/dimethyl sulfoxide (PAN/DMSO) solution to fine-tune the properties of the PAN spinning dope (39). Our results showed that a small amount of graphene was able to reduce the porosity and enhance the mechanical properties of the PAN/graphene composite CFs. PAN/graphene-based CFs with 0.075 wt % graphene exhibited a tensile strength of 1916 MPa and Young's modulus of 233 GPa, which represented a 225% increase in strength and 184% increase in modulus compared to PAN CFs without graphene. Atomistic ReaxFF calculations and large-scale molecular dynamics (MD) simulations jointly elucidated the microstructure modification mechanism of graphene. The simulation results show that the addition of graphene introduces favorable edge chemistry, promotes carbon content, enhances polymer chain alignment, and increases crystallinity. These insights not only expand the understanding of PAN-based CF production but also provide a foundation for developing low-cost alternative precursor fibers enhanced by graphene, which may yield CFs that are competitive with or superior to PAN-based CFs and cost less.

## RESULTS

PAN fibers produced on a lab-scale wet spinning line (Fig. 1A) showed that the addition of graphene to the PAN/DMSO dope substan-

tially changed the fiber microstructure and increased the strength, Young's modulus, and strain of the resultant PAN/graphene composite CFs. Scanning electron microscopy (SEM) images of the carbonized PAN/graphene CFs, as shown in Fig. 1 (C to G), revealed that the addition of graphene significantly reduced the size of pores and voids in the fiber compared to PAN-based CFs produced without graphene, as shown in Fig. 1B.

The best mechanical properties of the PAN/graphene composite CFs were achieved at a graphene concentration of 0.075 wt % (PAN/graphene-0.075), which exhibited a tensile strength of 1916 MPa and Young's modulus of 233 GPa. These results are 225 and 184% greater than the strength (589 MPa) and modulus (82 GPa) exhibited by the PAN CF control sample (Fig. 1H). At the same time, the fracture strain remained largely unaffected by the presence of graphene up to the concentration of 0.075 wt % (Fig. 1I). However, when the concentration of graphene increased to 0.1 wt %, the PAN/graphene composite CFs exhibited a reduced strength of 980 MPa and a fracture strain of 0.6%. Similar results have been reported for CNTs and other graphene polymer systems. Some reports showed that a low concentration of CNTs/graphene (less than 1.0 wt %) could significantly enhance the mechanical properties. However, after passing a critical content, the mechanical properties of the composites start to deteriorate as CNT/graphene concentration increase (30, 40).

Nanotomography with 17-nm voxel resolution was used to unveil the role of graphene in regulating the porosity of carbonized fibers (Fig. 2). PAN-based CFs produced through the lab-scale spin line without graphene exhibited elongated axial micropores with a typical diameter of ~300 nm and a length of 3  $\mu\text{m}$ , as denoted by the orange ellipses. Increasing graphene content reduced the prevalence of elongated axial micropores as shown in Fig. 2 (A to C). When the graphene concentration increased to 0.1 wt %, almost all axial micropores had disappeared (Fig. 2D). Elimination of the large pore had clear mechanical benefits by increasing the effective load-bearing cross section in the specimens. However, the PAN/graphene-0.1 (0.1 wt % graphene addition) sample exhibited abundant spherical nanoporosity with characteristic diameters of ~150 nm (as seen from the amplified view of a porous region shown in the inset in Fig. 2D), which negatively affected the strength of the fibers. The role of these two different classes of pores can be assessed in the framework of the maximum principal stress failure criterion, which states that failure of the brittle solid occurs when the local principal stress exceeds the material strength. The aspect ratio of the void contributes significantly to the stress concentration and thus the overall fiber strength as demonstrated analogously by an elliptical hole in an infinite plate (Fig. 2F). The well-known Inglis solution for this problem shows that the maximum axial stress occurs at the horizontal tip of the ellipse (41)

$$\sigma_y = \sigma_o \left( 1 + 2 \frac{a}{b} \right) \quad (1)$$

Notably, the stress concentration ( $\sigma_y$ ) depends only on the pore aspect ratio ( $a/b$ ; as illustrated in Fig. 2F) and far-field stress ( $\sigma_o$ ) and is not affected by the pore size. Using representative values for the elongated microporosity in the low graphene-containing fibers (<0.075 wt %), we find a stress concentration of

$$\sigma_y^{\text{macro}} \approx 1.2 \sigma_o \quad (2)$$

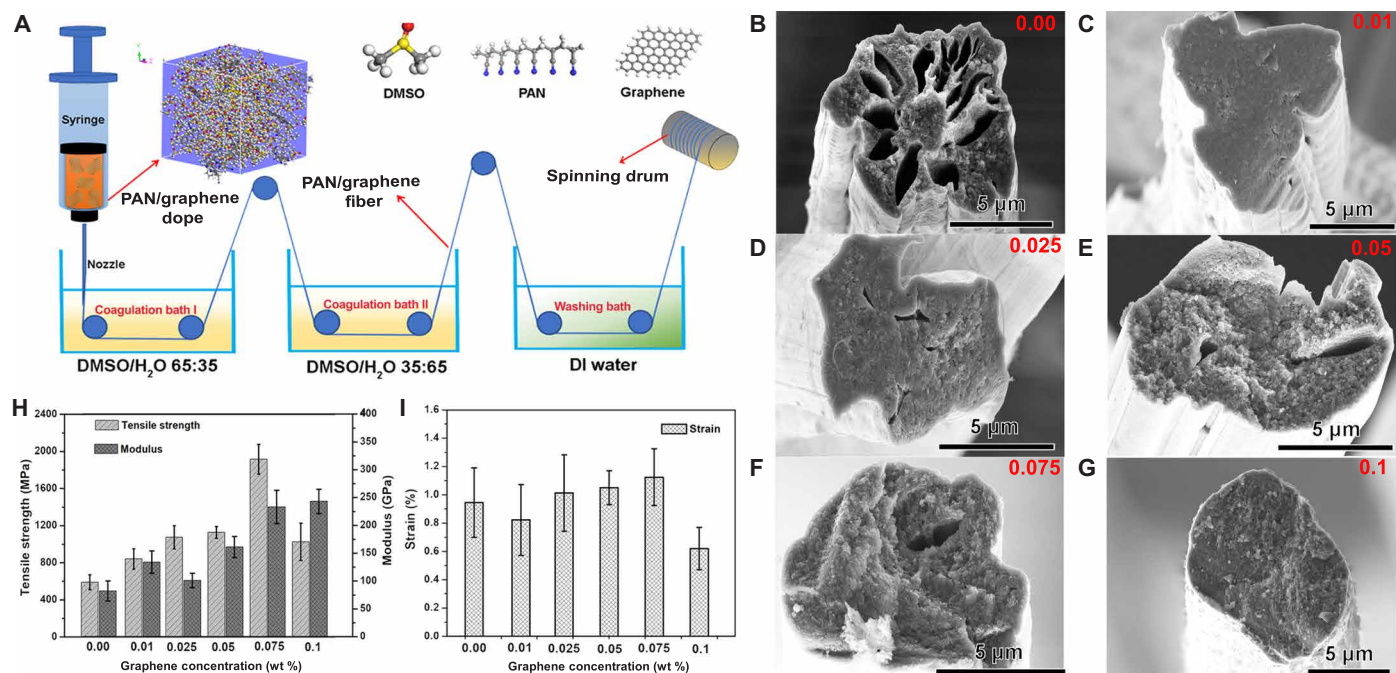


**Fig. 1. Illustration of the wet spinning process, microstructure, and mechanical properties of the PAN/graphene composite CFs.** (A) Illustration of the fabrication process of PAN/graphene precursor fibers. DI, deionized. (B to G) SEM images of the carbonized PAN/graphene composite fibers with different weight percentage of graphene, (B) 0.00 wt %, (C) 0.01 wt %, (D) 0.025 wt %, (E) 0.05 wt %, (F) 0.075 wt %, and (G) 0.1 wt %. (H and I) Mechanical properties of the carbonized PAN/graphene CFs with different graphene concentration.

Similarly, for the equiaxed nanoporosity in the PAN/graphene-0.1 fiber, the stress concentration is

$$\sigma_y^{\text{nano}} \approx 3\sigma_0 \quad (3)$$

As a result, the equiaxed nanoporosity observed at high graphene concentration (0.1 wt %) is more detrimental to the fiber strength than the elongated pores observed at lower graphene concentration (0.075 wt %). Thus, the best properties are obtained at a moderate graphene concentration that eliminates microporosity without introducing nanoporosity.

These results clearly show that graphene modifies both the microstructure and mechanical performance of CFs; however, it was unclear how graphene achieves this effect. The addition of graphene may affect the final CF at several stages of the production cycle. For example, (i) the addition of graphene may affect the rheological properties of the spinning dope and lead to different properties; (ii) as illustrated in Fig. 3G, the extrusion forces on the spinning dope may help align the graphene nanosheets along the flow direction (33); (iii) graphene may serve as a reinforcement to increase the mechanical properties; (iv) tension in the spinning line may align the polymer chain, which includes the graphene nanosheets, along the fiber axis; and (v) the shrinkage of the fiber during the solidification and drying process may cause the graphene nanosheets to align and facilitate local ordering in the microstructure of PAN/graphene fiber.

The above-proposed mechanisms were systematically investigated by examining the viscosity of the spinning dope, the morphology, graphene distribution, polymer alignment, and the mechanical properties of the PAN/graphene fibers after each processing step. Photographs and the corresponding viscosity of the PAN/graphene/DMSO spinning dope are given in fig. S1. The color of the spinning dope

became darker as the graphene concentration increased (fig. S1A). From fig. S1 (B and C), the viscosity of the PAN/graphene spinning dope gradually increased when the graphene concentration increased from 0.01 to 0.075 wt %, reflecting the increasing interaction between graphene nanosheets and PAN polymer chains. When the concentration of graphene was further increased to 0.1 wt %, a decreased viscosity was observed, which can be attributed to the onset of lubrication effects at high graphene concentration. At low concentrations, the increased viscosity of the spinning dope might help align the graphene nanosheets along the fiber direction during the spinning process due to larger shear stress. Therefore, it can be inferred that the well-aligned graphene nanosheets guide the solidification of PAN molecules during the coagulation process, helping minimize the large pores and voids.

Transmission electron microscopy (TEM) images of graphene shear-exfoliated from graphite demonstrate a “wrinkled” structure of 2D graphene nanosheets (Fig. 3A). This wrinkling effect increases contact between the graphene and the polymer chains. The corresponding high-resolution TEM (HRTEM) image (Fig. 3B) and amplified image (inset of Fig. 3A) show the perfect hexagonal lattice structure of graphene, which can be further verified by the corresponding fast Fourier transform (FFT) pattern (inset of Fig. 3B). After the wet spinning process, the graphene nanosheets were found to be uniformly dispersed into the PAN matrix without any apparent agglomeration, which could be validated by the TEM image of the pure PAN and representative PAN/graphene-0.075 composite precursor fibers (fig. S2, A and B). Furthermore, many more dispersed crystal zones were observed in the PAN/graphene-0.075 fiber (fig. S2B) compared to the pure PAN fiber (fig. S2A). These crystal flakes feature the hexagonal crystal lattice of graphene as determined by the corresponding FFT pattern (inset of Fig. 3C).

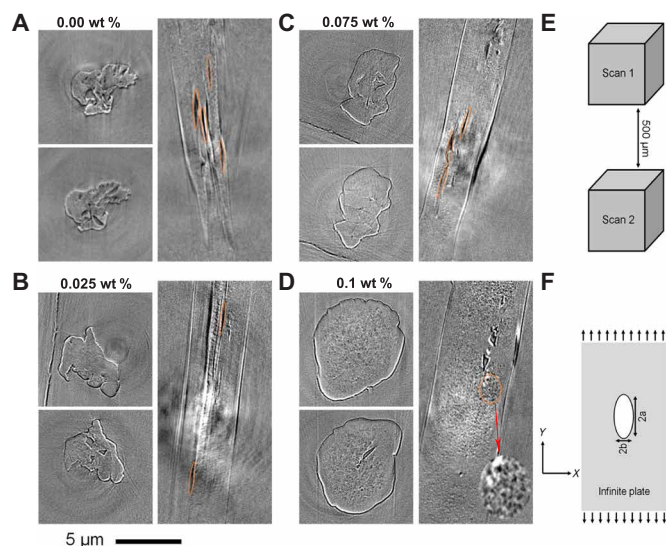


**Fig. 2. Nanotomography measurement of PAN/graphene composite CFs.** Images are shown for different levels for graphene content: (A) 0.00 wt %, (B) 0.025 wt %, (C) 0.075 wt %, and (D) 0.1 wt %. (E) Each panel shows two axial cross sections located at different positions on the fiber length. (F) 2D model of elliptical hole in infinite plate.

After oxidation and carbonization, these crystal zones of graphene are retained inside the PAN/graphene composite CFs, as shown in the TEM and HRTEM images of PAN/graphene-0.075 in Fig. 3 (D and E). The graphene nanosheets are surrounded by the turbostratic graphitic structure developed by the carbonization of the ladder structure of the PAN polymer chain. Raman spectra of the PAN/graphene composite CFs are given in Fig. 3F, which has been widely used to characterize the ordered/disordered structure of graphitic materials. Typically, the  $D$  band at  $1350\text{ cm}^{-1}$  results from the breathing mode of point photons of  $A_{1g}$  symmetry, representing the defects and disordered graphite structures, while the  $G$  band at  $\sim 1585\text{ cm}^{-1}$  is ascribed to the first-order scattering of the  $E_{2g}$  phonon mode of in-plane  $sp^2$  C atoms. The ratio between  $D$  and  $G$  peak intensities, denoted as  $I_D/I_G$ , is used as a measure of the quantity of ordered graphitic structures (42, 43). The lower  $I_D/I_G$  of the PAN/graphene-0.075 composite CF suggests reduced defects, more ordered graphitic structure, as well as higher crystal orientation along the fiber axis. Figure S2C compares the x-ray diffraction (XRD) patterns of the prepared PAN fiber after each processing step. The sharp and intense diffraction of the untreated pure PAN fibers at  $\sim 17^\circ$  corresponds to the (200) crystal plane of PAN (44). After oxidation, the sharp (200) peak becomes wider, which may be due to the interaction of PAN molecules and the formation of the ladder structure during the oxidation process. A weak and broad peak can be detected at around  $24^\circ$  for the carbonized PAN fiber and all of the PAN/graphene composite fibers (fig. S2D), which is ascribed to the (002) plane of the graphitic structure.

The effect of graphene on the performance of PAN/graphene composite precursor fiber was investigated by comparing the thermal degradation, microstructure, and mechanical properties of the PAN/graphene composite fibers to those of pure PAN fibers. Figure S3 shows the thermogravimetric analysis (TGA) curves of the pure PAN and PAN/graphene composite precursor fibers. TGA is a quantitative method to measure the amount of moisture and volatile

compounds present in nanocomposite fibers, calculate the weight loss during thermal processing, and determine mechanisms of thermal degradation. The programmed heating profile is shown in fig. S3C, which is used to mimic the oxidation and carbonization processes. Both pure PAN and PAN/graphene composite precursor fibers demonstrated a similar thermal degradation trend, as shown in fig. S3 (A, B, and D). No weight loss was observed for both PAN and PAN/graphene precursor fibers from room temperature to  $200^\circ\text{C}$ , which indicates the cyclization process of the PAN molecule chain. However, a 0.5 wt % weight gain was observed in the PAN/graphene-0.075 composite precursor fiber at the initial heating stage (fig. S3A), which can be attributed to the reaction of oxygen and PAN polymer, as well as the possible attachment of oxygen with Nitrile group. The large surface area of graphene may facilitate the attachment and reaction between PAN and oxygen (45). During the 2-hour holding time at  $250^\circ\text{C}$  (fig. S3B), significant weight loss was observed for both PAN and PAN/graphene-0.075 composite fibers, which is due to the release of small gas molecules. When the temperature was increased to  $950^\circ\text{C}$ , both PAN and PAN/graphene-0.075 composite fibers showed a similar thermal degradation process (fig. S3D), with final carbon yield of 37.56% for PAN/graphene-0.075 fibers and 36.41% for PAN fibers. TGA results demonstrated that graphene facilitated the interaction between PAN polymer chain and oxygen and slightly increased the final carbon content.

Fiber characterization was performed at each step of CF production to trace the effect of graphene on the fiber's microstructure and mechanical properties. Figure S4 compares the microstructure and mechanical properties of the precursor fibers before oxidation. The pure PAN precursor fiber showed a highly porous structure (fig. S4A), while the PAN/graphene precursor fibers exhibited denser microstructure (fig. S4, B to F) and improved mechanical properties (fig. S4, G to I). However, the graphene concentration and the enhancement of the mechanical properties are not directly proportional; when the graphene concentration was increased to 0.1 wt %, the precursor fiber demonstrated reduced ductility, as evidenced by the drop in the fracture strain (fig. S4I). Figure S5 compares the microstructure and mechanical properties of the precursor fibers after oxidation. A similar trend was observed in the oxidized PAN and PAN/graphene fibers (fig. S5, A to F), especially for the PAN/graphene-0.1 sample where the pulled-out graphene nanosheets could be observed on the cross-sectional SEM image of the fracture surface (inset of fig. S4F). The oxidized PAN/graphene composite fibers showed greater strength and modulus but significantly reduced fracture strain compared to PAN/graphene precursor fibers, as shown in fig. S5 (G to I). The best mechanical properties were also achieved in the oxidized fibers with 0.075 wt % graphene. Last, the carbonization step leads to a marked increase in strength and ductility and a further decrease in fracture strain. Figure S6 compares the mechanical properties of pure PAN and PAN/graphene-0.075 composite fibers after each processing step, which clearly shows that 0.075 wt % graphene has a significant increase in strength (from 589 to 1919 MPa) and modulus (from 82 to 233 GPa). These experimental results of the PAN and PAN/graphene fibers in the as-spun, oxidized, and carbonized states indicate that graphene can modify the microstructure of PAN fibers at the initial spinning stage and lead to PAN/graphene fibers with better mechanical properties after carbonization. Note that the concentration of graphene should be maintained at an appropriate level: After exceeding a critical value, the added graphene might damage fiber's mechanical properties.

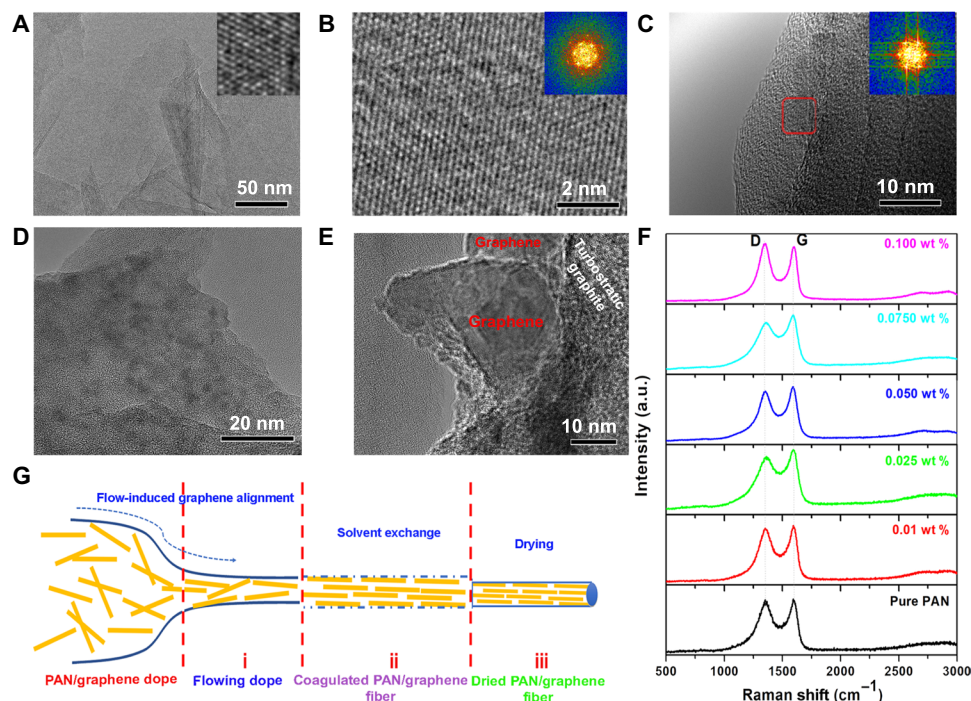


**Fig. 3.** TEM images and Raman spectra of the PAN/graphene composite CFs. (A) TEM images of the added graphene obtained from shear exfoliation. (B) HRTEM image of the graphene, with inset showing the corresponding FFT pattern. (C) TEM image of PAN/graphene (0.075 wt %) precursor fiber, with inset showing the FFT pattern of the selected area (red square). (D and E) TEM images of the carbonized PAN/graphene fiber (0.075 wt % graphene) at different magnifications. (F) Raman spectra of the carbonized PAN/graphene fibers with different concentrations of graphene. a.u., arbitrary unit. (G) The possible flow-induced graphene alignment mechanism of the PAN/graphene dope (33).

Encouraged by these experimental results, atomistic ReaxFF simulations and large-scale MD simulations were performed to achieve a deeper understanding of how graphene affects the microstructure and enhances the mechanical properties of PAN fibers. The goal is to explore the interaction between graphene and the PAN polymer chains during each processing step. The effect of graphene on the reaction chemistry, small gas molecular emission, carbon ring formation and distribution, molecular alignment, and crystallinity was examined to unveil the role of graphene in the PAN/graphene composite fiber.

In particular, atomistic ReaxFF was used to study the effect of graphene on the chemistry of PAN-based CFs, which can provide information on the release of gas molecules and the formation of carbon rings during the carbonization process. The results of these simulations indicate that the addition of a small amount of graphene into the polymer matrix does not significantly increase the production of gas molecules ( $H_2/H_2O/N_2/CO/CO_2$ ) (Fig. 4, A to C, and fig. S7). Therefore, the carbon content of PAN/graphene CFs remains comparable to that of PAN CFs during the carbonization process, while both oxidized PAN and oxidized PAN/graphene show a significant increase of carbon content with the increased reaction time (Fig. 4G). After 900 ps, the carbon contents calculated by ReaxFF MD for PAN and PAN/graphene CFs are  $\sim 81.5$  and  $\sim 82\%$  respectively (Fig. 4G). Overall, the PAN/graphene sample shows slightly higher carbon content than that of pure PAN sample, which agrees with the experimental TGA result (fig. S3D). The simulation results also show that adding graphene to the PAN precursor does not significantly affect the formation of 5/6/7-membered carbon rings. Because of their conjugated  $sp^2$  electronic configuration, the surface carbon atoms of graphene are relatively inactive. However, there are

dangling bonds on the graphene edges, which make the graphene edges capable of forming bonds with the polymer matrix and providing catalytic seeds for the formation of larger graphitic structure (Fig. 4, D to F). The graphene nanosheets are found to exhibit favorable edge chemistry with the formation of 5/6/7-membered carbon rings only at the graphene edges, not at the graphene surface (Fig. 4, H and I). Furthermore, the added graphene also improves the alignment of 6-membered carbon rings. Using Herman's orientation function (HOF) to measure the alignment shows 12% greater alignment in PAN/graphene CFs than that of PAN CFs (fig. S8), which explains the effect of graphene on the microstructure of PAN/graphene CFs.

To further investigate the effect of graphene on the alignment of PAN chains, we performed large-scale nonreactive MD simulations of structures containing PAN chains and graphene sheet. Figure 5 (A and B) shows the final configurations of structures with and without graphene obtained by the end of 7.5-ns-long heating-annealing-cooling simulations, as detailed in Materials and Methods. The snapshots show the positions of ring centers of PAN chains instead of positions of atoms. Each ring is colored based on its orientation with respect to the  $z$  axis, which is normal to the plane of graphene sheet in the initial structure (fig. S9B). Adjacent ring centers are joined by a line. The alignment of PAN rings with respect to the graphene sheet decreases as color changes from pink to red. Figure 5C shows the orientation distribution of rings that belong to the graphene sheet of PAN/graphene structure, while Fig. 5 (D and E) shows the ring orientation distributions of PAN/graphene and PAN structures, respectively. Note that rings belonging to the graphene sheet are not included in Fig. 5D. It can be seen that the graphene sheet undergoes some wrinkling during the MD simulation due to its interactions with PAN chains (Fig. 5A). When compared

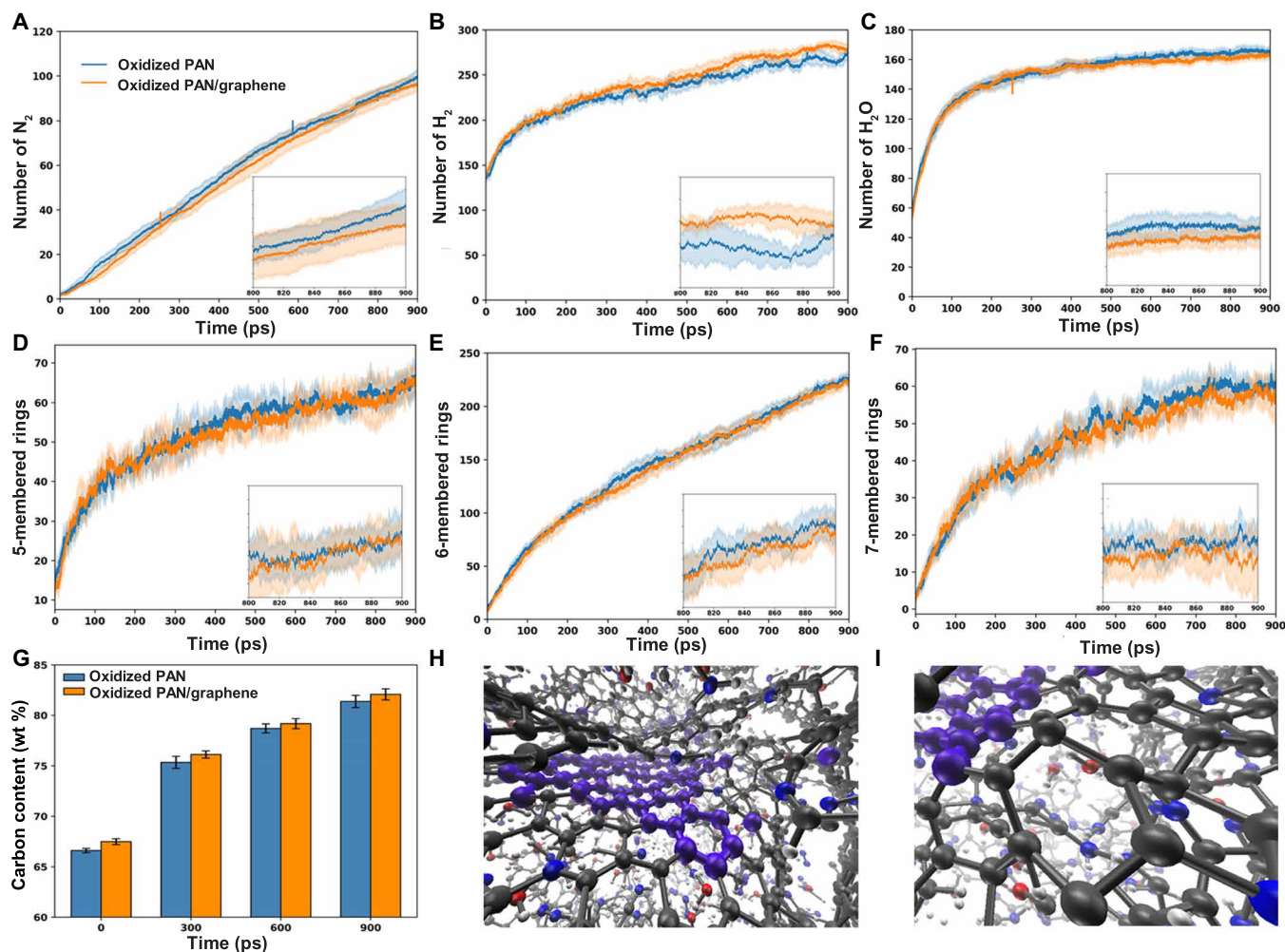


**Fig. 4. Atomistic ReaxFF simulations of the initial stage of carbonization process for oxidized PAN and oxidized PAN/graphene precursors.** Production of (A)  $N_2$ , (B)  $H_2$ , (C)  $H_2O$  molecules. Formation of (D) 5-, (E) 6-, and (F) 7-membered carbon rings. (G) Carbon content of fibers at different simulation times for the oxidized PAN and oxidized PAN/graphene precursors. (H and I) Snapshots of the oxidized PAN/graphene taken during the carbonization process to show the formation of 5/6/7-membered carbon-only rings at the graphene edges. Carbon, nitrogen, oxygen, and hydrogen are represented black, blue, red, and white, respectively. Purple spheres represent the initial graphene structure. Dark lines and shadows in (A) to (F) are the average and SD over eight different samples, respectively. Insets (A) to (F) show simulation results for the last 100 ps.

to the initial state (HOF = 1.0), the graphene sheet's overall orientation mostly remains unchanged (HOF = 0.94) with most of the ring normals still parallel to the  $z$  axis (Fig. 5C). The presence of graphene causes PAN chains to undergo considerable local realignment. During this realignment, the orientation distribution of PAN chains gets narrower (Fig. 5D), and overall HOF changes from the initial value of  $-0.052$  to the final value of  $0.53$ . Hence, the PAN/graphene structure has a much higher degree of alignment, with a significant portion of PAN chains aligned along the graphene sheet. In the absence of graphene, HOF value of PAN chains changes nominally to  $0.06$ , and the orientation distribution of PAN chains remains flat (Fig. 5E). Hence, the PAN structure has poor alignment when compared to PAN/graphene structure.

Furthermore, we divided the computational cell into 20 bins along the  $z$  axis (perpendicular to graphene sheet) and calculated the HOF value of each bin by averaging over all rings that are part of a bin to demonstrate how graphene affect the PAN chain alignment. Figure 5F shows the variation of HOF in the  $z$  direction for

initial and annealed PAN and PAN/graphene structures. Similar to Fig. 5D, rings belonging to the graphene sheet are excluded from this analysis. For the PAN structure, most of the bins have HOF values lower than  $0.2$ , which indicates that PAN chains have a random orientation in most parts of the computational cell. However, for the PAN/graphene system, nearly 80% of bins have HOF values higher than  $0.4$ , which indicates that the alignment of carbon rings along the graphene sheet occurs throughout the computational cell. In addition, the rings that are within  $5$  nm of the graphene sheet show a considerably higher degree of alignment ( $0.8 < \text{HOF} < 1.0$ ). Figure 5A further shows that these thin crystallites of highly aligned chains grow deeper than  $10$  nm in some locations of the computational cell. These results clearly show that graphene plays a significant role in enhancing the overall alignment of PAN chains. Earlier reactive simulations of carbonization and graphitization processing steps suggest that the enhanced alignment of PAN chains translates to the corresponding alignment of graphene sheets and an increased fraction of graphitic phase in the CF microstructure (46). These

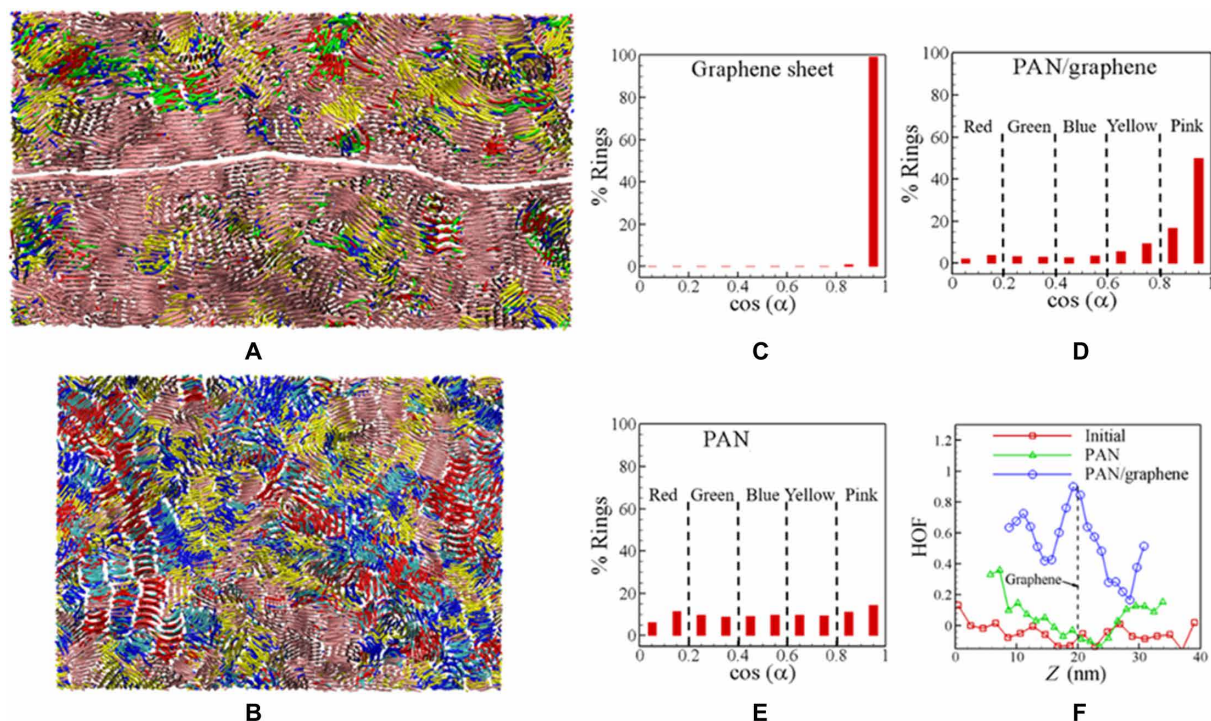


**Fig. 5. Nonreactive MD simulations of structural self-organization of PAN chains with and without the presence of a graphene sheet.** Snapshots (A and B), ring orientation distributions (C to E), and HOF distributions (F) of PAN/graphene and PAN structures. In the snapshots of PAN/graphene and PAN structures, individual PAN chains are shown by lines joining carbon ring centers. For PAN/graphene structure, the horizontal gap in the middle of the system corresponds to the graphene sheet, which is not shown for visualization purposes. The ring centers are colored according to the cosine angles of ring normal vectors with respect to the vertical  $z$  axis. The color scheme is shown in (D) and (E).

structural changes lead to the improvement of Young's modulus and tensile strength of CFs, as has been demonstrated in the computational tensile testing of several simulated microstructures (46) and in the experimental study reported in the present paper.

## DISCUSSION

In this work, a small amount of shear-exfoliated graphene was introduced into the PAN/DMSO to tune the properties of the spinning dope and control the microstructure of the PAN/graphene composite CFs. Our results demonstrated that including 0.075 wt % graphene in PAN precursor fibers significantly reduced porosity and enhanced mechanical properties, with a 225% increase in strength and a 184% increase in Young's modulus. The enhancements in both strength and modulus can be attributed to the following factors: (i) the addition of graphene nanosheets improves the microstructure of the PAN/graphene composite CF through minimization of the size of voids/defects inside the PAN/graphene precursor fibers and improved alignment of structural elements of the microstructure at all stages of CF manufacturing; and (ii) the graphene serves as a reinforcing phase to further improve the mechanical properties. Atomistic ReaxFF and large-scale MD simulations were used to elucidate the mechanisms that define the effect of graphene of the CF microstructure. ReaxFF simulations demonstrated the unique graphene-induced edge chemistry, which favored the formation of 5/6/7-membered carbon rings along the graphene edges. The addition of graphene also increased the alignment of six-member rings and slightly increased the carbon yield during the carbonization

process. Large-scale MD simulations further confirmed the increased alignment of PAN polymer rings along the graphene sheets, which increased the crystallinity of composite CFs and enhanced the mechanical properties. Unveiling these mechanisms has opened the door to the development of alternative precursors for low-cost CFs.

## MATERIALS AND METHODS

### Preparation of graphene nanosheets and PAN/graphene spinning dope

All of the chemicals and materials were used without further purification after purchase. Graphene was prepared through a modified shear exfoliation method using a Silverson Machines L5M-A high-speed, high-shear laboratory mixer. Typically, 0.5-g graphite flakes (Sigma-Aldrich) were dispersed into 100 ml of DMSO solution (anhydrous,  $\geq 99.9\%$ ; Sigma-Aldrich). The graphite/DMSO solution was then shear mixed at 3500 revolutions per minute (rpm) for 12 hours. Next, the shear-exfoliated graphene/DMSO solution with mono/multilayered graphene nanosheets was sonicated for 1 hour (Branson ultrasonic cleaner) and then centrifuged (Col-Int Tech, Centrifuge TDL60) at 1500 rpm to remove any remaining unexfoliated graphite. The concentration of the obtained DMSO/graphene solution was calculated by weighing the dry sample from 10 ml of DMSO/graphene after evaporation.

The PAN/graphene spinning dope was prepared with 7.5 g of PAN (mean particle size, 50  $\mu\text{m}$ ; copolymer, 99.5% acrylonitrile (AN)/0.5% methyl acrylate (MA); molecular weight, 230  $\text{kg mol}^{-1}$ ; Goodfellow) and synthesized graphene powder in 100 ml of DMSO

solvent. The added graphene nanosheets have a thickness of  $\sim 0.8$  nm and an average lateral size of 300 nm, as shown from the atomic force microscopy (AFM) image in fig. S10. To prevent the aggregation of the exfoliated graphene nanosheets, DMSO was selected as the solvent to stabilize and disperse the exfoliated pristine graphene sheets due to its strong affinity for graphene (47). In this work, the concentration of the added graphene was controlled under 0.1 wt % to improve the dispersion and prevent the agglomeration of graphene nanosheets in PAN polymer. The weight percentage of graphene in the PAN/graphene composite precursor fiber was controlled at 0.00, 0.01, 0.025, 0.05, 0.075, and 0.1 wt %, which are hereafter denoted as PAN/graphene-0.00, PAN/graphene-0.01, PAN/graphene-0.025, PAN/graphene-0.05, PAN/graphene-0.075, and PAN/graphene-0.1, respectively. The PAN/graphene dope was then heated to 60°C for 2 hours under continuous stirring. The solid concentration of the PAN/DMSO dope was about 7.5 wt %.

### Wet spinning of PAN/graphene composite precursor fibers

A lab-scale, single-filament wet spinning line was assembled to produce the aforementioned PAN/graphene precursor fibers. The PAN/graphene dope was extruded through a 5-ml syringe with a 110- $\mu\text{m}$ -diameter needle by a syringe pump. The fiber then traveled into two consecutive coagulation baths followed by a washing bath as illustrated in Fig. 1A. The solutions in coagulation baths I and II were DMSO/H<sub>2</sub>O (65:35) and DMSO/H<sub>2</sub>O (35:65) mixtures, respectively. The draw ratio was controlled by adjusting the speed of the syringe pump, guiding rollers, and take-up drum (table S1). With the help of the guided rollers, the solidified PAN/graphene filaments were further stretched and washed to form the PAN/graphene composite precursor fibers. The total draw ratio from the nozzle to the final PAN/graphene precursor fiber was about 10. Last, the collected precursor PAN/graphene fibers were dried at 80°C for 12 hours before the stabilization and carbonization processes.

### Stabilization and carbonization of PAN/graphene fibers

The PAN/graphene precursor fibers were batch process-stabilized using a box furnace (KSL-1200X-UL, MTI Inc.). A bundle of PAN/graphene fibers were heated to 250°C at a heating rate of 5°C/min and held for 2 hours. Tension was applied to the fiber bundles during stabilization to increase the alignment of the PAN polymer chain. The stabilized PAN/graphene fibers were then carbonized in a tube furnace (GSL-1700X-UL, MTI Inc.) at 1500°C with a heating rate of 5°C/min in argon atmosphere (200 standard cubic centimeter per minute) for 0.5 hours. The carbonized fibers were cooled to room temperature while continuously purging N<sub>2</sub> in the furnace.

### Characterization of PAN/graphene filaments and CFs

The cross sections and microstructures of the PAN/graphene composite fibers were characterized using SEM (FEI Quanta 650), TEM, and HRTEM (FEI Titan). The TEM samples were prepared by encasing a bundle of fibers in epoxy resin and then slicing 25- to 50- $\mu\text{m}$ -thick sections using a microtome (Leica, RM2155). The basic crystal and molecular structures of the carbonized PAN/graphene fibers were determined by XRD (pro multipurpose diffractometer equipped with Cu K $\alpha$  radiation with  $\lambda = 0.154$  06 nm) in the range of  $10^\circ < 2\theta < 80^\circ$ , Raman spectroscopy (Renishaw inVia Raman microscope at 514 nm with 5% laser power) in the range of 500 to 3200  $\text{cm}^{-1}$ . The height profile of the shear-exfoliated graphene was characterized by AFM (Dimension Icon with ScanAsyst, Bruker).

The viscosity of the spinning dope was measured on an Anton Paar MCR 301 rheometer with a parallel plate geometry, where the plate had a radius of 10 mm. The TGA of the PAN/graphene composite fibers was characterized by TGA Q50 (TA Instruments) in the range of 25° to 950°C. The 3D internal microstructure of the resulting CFs was resolved using transmission x-ray microscopy nanotomography at beamline 18-ID located at National Synchrotron Light Source II in Brookhaven National Laboratory. One fiber of each PAN concentration was imaged at 8 keV and reconstructed using the open-source TomoPy software to achieve an isotropic voxel size of 17.2 nm (48).

Tensile test specimens were prepared by using rectangular paper templates with a gauge length of 20 mm. The diameter of each specimen was measured by SEM after the tensile test. Tensile tests were conducted on a Nano-Tensile Tester–MTS Nano Bionix testing system with a 0.5-N load cell and a displacement rate of  $10^{-4}$   $\text{mm min}^{-1}$ .

### Atomistic ReaxFF MD simulation

Here, ReaxFF MD simulations were used to investigate the impact of graphene inclusion on PAN-based CFs at the atomistic level. The previous C/H/N force field parameters developed by Kamat *et al.* (49) were reoptimized against quantum mechanical data with an emphasis on N<sub>2</sub> chemistry. In contrary to the force field from Kamat *et al.* (49), N<sub>2</sub> molecules are sufficiently stable, thus do not react with carbon radicals. Therefore, frequent N<sub>2</sub> molecules removal during the simulations is not required (50). In addition, carbon parameters are more accurate for deriving the mechanical properties of graphene. Moreover, the force field is extended to C/H/O/N atoms widening its application to alternative polymer precursors such as stable oxidized PAN and PBO (poly(p-phenylene-2,6-benzobioxazole)). For a detailed description of this force field development process, see our previous published work (51).

In this work, a model depicting an oxidized PAN chain (fig. S9A, a) and a single-layer graphene sheet (16 Å × 16 Å) with hydrogen termination (fig. S9A, b) are used to construct our simulation systems after energy minimization. For the pure PAN system, 32 chains of oxidized PAN are randomly placed in the simulation box, while for the PAN/graphene system, a single-layer graphene sheet is located at the center of the box with 32 oxidized PAN chains positioned randomly. The periodic boundary condition is applied in all directions. The size of simulation cells is determined to provide an initial density of precursors equal to 1.6  $\text{g cm}^{-3}$  for all of the systems.

First, a 60-ps NVT simulation, where the number of molecules N, a volume of the system V and the temperature T = 300K is constant, is performed to equilibrate the systems (fig. S9A, c). Second, eight system configurations within the last 10 ps are heated up to 2800 K at a 10 K/ps rate to simulate the carbonization process. Third, the systems are kept at 2800 K for 900 ps for each trajectory. Note that the temperature difference between simulations and experiments (2800 and 1773 K for simulation and experiment, respectively) is meant to accelerate the reactions to a nanosecond time scale accessible to our simulations. The time step is 0.25 fs for each step of simulations and the total length of simulations is 1230 ps. A Berendsen-Anderson temperature thermostat with a damping constant of 100 fs was used. For each sample, we calculate the small molecule gas production, 5/6/7-carbon rings formation, and alignment during the carbonization step at 2800 K. The alignment of the systems is quantitatively calculated by using a HOF, which is defined as  $F = \frac{1}{2} [3\langle \cos^2 \theta \rangle] - 1$  where  $\theta$  is orientation relative to the axis of interest (52).

## Large-scale MD simulation

The PAN chain used in large-scale MD simulations is shown in fig. S9B, a. The chain is 2.1 nm long and consists of 10 six-member rings with one nitrogen atom in each ring. The graphene sheet contains 8000 carbon atoms and has dimensions of 41.9 nm in the longitudinal direction ( $x$  direction) and 4.8 nm in transverse direction ( $y$  direction). Since the size of experimental graphene flakes is much larger than the computational graphene sheet, the graphene sheet is modeled as infinite long in  $x$  and  $y$  directions by using periodic boundary conditions. The large-scale MD simulations are performed with (PAN/graphene) and without (PAN) graphene sheet. In building the initial configuration of PAN/graphene structure, the infinitely long graphene sheet is placed near the center of the computational cell ( $z = 20$  nm). The PAN chains are placed above and below the graphene sheet randomly using PACKMOL (53). The initial configuration of PAN/graphene system (fig. S9B, b) has a density of  $0.76 \text{ g/cm}^3$  and contains 2.5 wt % of graphene. The initial configuration of the PAN structure is obtained by removing the graphene sheet from the initial configuration of PAN/graphene system.

The large-scale nonreactive MD simulations are performed using polymer consistent force field (54) as implemented in Large-scale Atomic/Molecular Massively Parallel Simulator (LAMMPS) MD suite (55). The nonreactive simulations have been previously used for studying various polymer-based nanocomposites such as graphene/polythene (56), graphene/epoxy (57), and PAN/CNT (58). The initial configurations of both structures are equilibrated at  $27^\circ\text{C}$ . Then, an annealing-type MD simulation is performed on each structure, so ladders can rearrange themselves to thermodynamically favorable configuration. In the annealing-type simulation, each structure is heated from  $27^\circ$  to  $477^\circ\text{C}$  in 2.5 ns. Then, each structure is maintained at  $477^\circ\text{C}$  for 4 ns before cooling it down to  $27^\circ\text{C}$  in 1 ns. All MD simulations are performed using constant temperature-constant pressure ensemble (NPT, where  $N$  is the number of atoms,  $P$  is the pressure of the system, and  $T$  is the temperature of the system). The pressure was set to 1 atm in all MD simulations. The three orthogonal dimensions of the periodic computational cell are allowed to change independently in the pressure control algorithm (59). The MD simulations are performed with a time step of 0.5 fs. To quantify the effect of the graphene sheet on the polymer chain alignment, we calculated HOF using the orientation of six-member rings. The orientation of each ring is defined by a vector that is normal to the plane of a ring. In this approach, HOF value of 1.0 indicates the perfect alignment of rings with graphene sheet ( $z$  axis in simulations), and the HOF value of 0.0 indicates the random alignment of carbon rings. More details about the procedure used for calculating HOF can be found in (46).

## SUPPLEMENTARY MATERIALS

Supplementary material for this article is available at <http://advances.sciencemag.org/cgi/content/full/6/17/eaaz4191/DC1>

## REFERENCES AND NOTES

- X. Huang, Fabrication and properties of carbon fibers. *Materials* **2**, 2369–2403 (2009).
- E. Frank, L. M. Steudle, D. Ingildeev, J. M. Spörl, M. R. Buchmeiser, Carbon fibers: Precursor systems, processing, structure, and properties. *Angewandte* **53**, 5262–5298 (2014).
- E. Frank, F. Hermanutz, M. R. Buchmeiser, Carbon fibers: Precursors, manufacturing, and properties. *Macromol. Mater. Eng.* **297**, 493–501 (2012).
- L. Ma, Y. Zhu, P. Feng, G. Song, Y. Huang, H. Liu, J. Zhang, J. Fan, H. Hou, Z. Guo, Reinforcing carbon fiber epoxy composites with triazine derivatives functionalized graphene oxide modified sizing agent. *Compos. Part B Eng.* **176**, 107078 (2019).
- Y. Li, T. Zhang, B. Jiang, L. Zhao, H. Liu, J. Zhang, J. Fan, Z. Guo, Y. Huang, Interfacially reinforced carbon fiber silicone resin via constructing functional nano-structural silver. *Compos. Sci. Technol.* **181**, 107689 (2019).
- B. Song, T. Wang, L. Wang, H. Liu, X. Mai, X. Wang, N. Wang, Y. Huang, Y. Ma, Y. Lu, E. K. Wujcik, Z. Guo, Interfacially reinforced carbon fiber/epoxy composite laminates via in-situ synthesized graphitic carbon nitride ( $g\text{-C}_3\text{N}_4$ ). *Compos. Part B Eng.* **158**, 259–268 (2019).
- S. K. Nataraj, K. S. Yang, T. M. Aminabhavi, Polyacrylonitrile-based nanofibers—A state-of-the-art review. *Prog. Polym. Sci.* **37**, 487–513 (2012).
- A. H. Wazir, L. Kakakhel, Preparation and characterization of pitch-based carbon fibers. *N. Carbon Mater.* **24**, 83–88 (2009).
- J. M. Spörl, R. Beyer, F. Abels, T. Cwik, A. Müller, F. Hermanutz, M. R. Buchmeiser, Cellulose-derived carbon fibers with improved carbon yield and mechanical properties. *Macromol. Mater. Eng.* **1700195**, 1–10 (2017).
- J. F. Kadla, S. Kubo, R. A. Venditti, R. D. Gilbert, A. L. Compere, W. Griffith, Lignin-based carbon fibers for composite fiber applications. *Carbon* **40**, 2913–2920 (2002).
- S. Kubo, J. F. Kadla, Lignin-based carbon fibers: Effect of synthetic polymer blending on fiber properties. *J. Polym. Environ.* **13**, 97–105 (2005).
- N. Yusuf, A. F. Ismail, Post spinning and pyrolysis processes of polyacrylonitrile (PAN) -based carbon fiber and activated carbon fiber: A review. *J. Anal. Appl. Pyrolysis* **93**, 1–13 (2012).
- C. Xiang, N. Behabtu, Y. Liu, H. G. Chae, C. C. Young, B. Genorio, D. E. Tsentelovich, C. Zhang, D. V. Kosykin, J. R. Lomeda, C. C. Hwang, S. Kumar, M. Pasquali, J. M. Tour, Graphene nanoribbons as an advanced precursor for making carbon fiber. *ACS Nano* **7**, 1628–1637 (2013).
- O. P. Bahl, R. B. Mathur, K. D. Kundra, Structure of PAN fibers and its relationship to resulting carbon fibre properties. *Fibre Sci. Technol.* **13**, 147–151 (1981).
- D. D. Edie, The effect of processing on the structure and properties of carbon fibers. *Carbon* **36**, 345–362 (1998).
- S.-W. Lee, H.-Y. Lee, S.-Y. Jang, S. Jo, H.-S. Lee, W.-H. Choe, S. Lee, Efficient preparation of carbon fibers using plasma assisted stabilization. *Carbon* **55**, 361–365 (2013).
- J. Yang, Y. Liu, J. Liu, Z. Shen, J. Liang, X. Wang, Rapid and continuous preparation of polyacrylonitrile-based carbon fibers with electron-beam irradiation pretreatment. *Materials* **11**, E1270 (2018).
- L. Chen, C. Lu, F. Huang, H. Li, Y. Liu, Y. Lu, Doping boric acid into polyacrylonitrile fibers prior to drying process and the effects on stabilization. *J. Mater. Sci.* **52**, 9452–9464 (2017).
- J. Chen, C.-g. Wang, X.-g. Dong, H.-z. Liu, Study on the coagulation mechanism of wet-spinning PAN fibers. *J. Polym. Res.* **13**, 515–519 (2006).
- S. H. Bahrami, P. Bajaj, K. Sen, Effect of coagulation conditions on properties of poly(acrylonitrile-carboxylic acid) fibers. *J. Appl. Polym. Sci.* **89**, 1825–1837 (2003).
- A. I. Stoyanov, Influence of the content of polymer with different molecular weights in spinning solutions on properties of acrylic fibers. *J. Appl. Polym. Sci.* **27**, 235–238 (1982).
- D.-G. Yu, W.-L. Chou, M.-C. Yang, Effect of bore liquid temperature and dope concentration on mechanical properties and permeation performance of polyacrylonitrile hollow fibers. *Sep. Purif. Technol.* **51**, 1–9 (2006).
- X. Zeng, J. Hu, J. Zhao, Y. Zhang, D. Pan, Investigating the jet stretch in the wet spinning of PAN fiber. *J. Appl. Polym. Sci.* **106**, 2267–2273 (2007).
- H. G. Chae, M. L. Minus, S. Kumar, Oriented and exfoliated single wall carbon nanotubes in polyacrylonitrile. *Polymer* **47**, 3494–3504 (2006).
- H. G. Chae, Y. H. Choi, M. L. Minus, S. Kumar, Carbon nanotube reinforced small diameter polyacrylonitrile based carbon fiber. *Compos. Sci. Technol.* **69**, 406–413 (2009).
- T. V. Sreekumar, T. Liu, B. G. Min, H. Guo, S. Kumar, R. H. Hauge, R. E. Smalley, Polyacrylonitrile single-walled carbon nanotube composite fibers. *Adv. Mater.* **16**, 58–61 (2004).
- H. G. Chae, M. L. Minus, A. Rasheed, S. Kumar, Stabilization and carbonization of gel spun polyacrylonitrile/single wall carbon nanotube composite fibers. *Polymer* **48**, 3781–3789 (2007).
- D. Papkov, A. M. Beese, A. Goponenko, Y. Zou, M. Naraghi, H. D. Espinosa, B. Saha, G. C. Schatz, A. Moravsky, R. Loutfy, S. T. Nguyen, Y. Dzenis, Extraordinary improvement of the graphitic structure of continuous carbon nanofibers templated with double wall carbon nanotubes. *ACS Nano* **7**, 126–142 (2013).
- S. Stankovich, D. A. Dikin, G. H. B. Dommett, K. M. Kohlhaas, E. J. Zimney, E. A. Stach, R. D. Piner, S. B. T. Nguyen, R. S. Ruoff, Graphene-based composite materials. *Nature* **442**, 282–286 (2006).
- V. Balaji, K. Lau, D. Hui, D. Bhattacharyya, Graphene-based materials and their composites: A review on production, applications and product limitations. *Compos. Part B* **142**, 200–220 (2018).
- Y. Zhang, Z. Gao, N. Song, J. He, X. Li, Graphene and its derivatives in lithium-sulfur batteries. *Mater. Today Energy* **9**, 319–335 (2018).
- K. Sun, J. Dong, Z. Wang, Z. Wang, G. Fan, Q. Hou, L. An, M. Dong, R. Fan, Z. Guo, Tunable negative permittivity in flexible graphene/PDMS metacomposites. *J. Phys. Chem. C* **123**, 23635–23642 (2019).
- Z. Xu, C. Gao, Graphene fiber: A new trend in carbon fibers. *Mater. Today* **18**, 480–492 (2015).
- Z. Xu, Y. Liu, X. Zhao, L. Peng, H. Sun, Y. Xu, X. Ren, C. Jin, P. Xu, M. Wang, C. Gao, Ultrastiff and strong graphene fibers via full-scale synergetic defect engineering. *Adv. Mater.* **28**, 6449–6456 (2016).

35. A. T. Chien, H. C. Liu, B. A. Newcomb, C. Xiang, J. M. Tour, S. Kumar, Polyacrylonitrile fibers containing graphene oxide nanoribbons. *ACS Appl. Mater. Interfaces* **7**, 5281–5288 (2015).
36. F. Meng, W. Lu, Q. Li, J. H. Byun, Y. Oh, T. W. Chou, Graphene-based fibers: A review. *Adv. Mater.* **27**, 5113–5131 (2015).
37. B. V. Cunnning, B. Wang, T. J. Shin, R. S. Ruoff, Structure-directing effect of single crystal graphene film on polymer carbonization and graphitization. *Mater. Horiz.* **6**, 796–801 (2019).
38. S. Sayyar, J. Moskowitz, B. Fox, J. Wiggins, G. Wallace, Wet-spinning and carbonization of graphene/PAN-based fibers: Toward improving the properties of carbon fibers. *J. Appl. Polym. Sci.* **136**, 47932 (2019).
39. K. R. Paton, E. Varrla, C. Backes, R. J. Smith, U. Khan, A. O'Neill, C. Boland, M. Lotya, O. M. Istrate, P. King, T. Higgins, S. Barwich, P. May, P. Puczkarski, I. Ahmed, M. Moebius, H. Pettersson, E. Long, J. Coelho, S. E. O'Brien, E. K. McGuire, B. M. Sanchez, G. S. Duesberg, N. McEvoy, T. J. Pennycook, C. Downing, A. Crossley, V. Nicolosi, J. N. Coleman, Scalable production of large quantities of defect-free few-layer graphene by shear exfoliation in liquids. *Nat. Mater.* **13**, 624–630 (2014).
40. G. Mittal, V. Dhand, K. Y. Rhee, S.-J. Park, W. R. Lee, A review on carbon nanotubes and graphene as fillers in reinforced polymer nanocomposites. *J. Ind. Eng. Chem.* **21**, 11–25 (2015).
41. C. E. Inglis, Stresses in a plate due to the presence of cracks and sharp corners. *Transactions of the Institution of Naval Architects* **55**, 219–230 (1913).
42. L. G. Cançado, A. Jorio, E. H. M. Ferreira, F. Stavale, C. A. Achete, R. B. Capaz, M. V. O. Moutinho, A. Lombardo, T. S. Kulmala, A. C. Ferrari, Quantifying defects in graphene via Raman spectroscopy at different excitation energies. *Nano Lett.* **11**, 3190–3196 (2011).
43. A. Eckmann, A. Felten, I. Verzhbitskiy, R. Davey, C. Casiraghi, Raman study on defective graphene: Effect of the excitation energy, type, and amount of defects. *Phys. Rev. B* **88**, 035426 (2013).
44. D. C. Onwudiwe, C. A. Strydom, R. M. K. Vala, L. Tichagwa, Preparation and structural properties of electrospun PAN nanofibers reinforced with ZnS nanoparticles. *Synth. React. Inorganic* **45**, 1251–1259 (2015).
45. W. S. Khan, M. Ceylan, L. Saednia, R. Asmatulu, Chemical and thermal investigations of electrospun polyacrylonitrile nanofibers incorporated with various nanoscale inclusions. *J. Therm. Eng.* **3**, 1375–1390 (2017).
46. K. Joshi, M. I. Arefev, L. V. Zhigilei, Generation and characterization of carbon fiber microstructure in atomistic simulations. *Carbon* **152**, 396–408 (2019).
47. C.-J. Shih, S. Lin, M. S. Strano, D. Blankschtein, Understanding the stabilization of liquid-phase-exfoliated graphene in polar solvents: Molecular dynamics simulations and kinetic theory of colloid aggregation. *J. Am. Chem. Soc.* 14638–14648 (2010).
48. D. Gürsoy, F. De Carlo, X. Xiao, C. Jacobsen, TomoPy: A framework for the analysis of synchrotron tomographic data. *J. Synchrotron Radiat.* **21**, 1188–1193 (2014).
49. A. M. Kamat, A. C. T. van Duin, A. Yakovlev, Molecular dynamics simulations of laser-induced incandescence of soot using an extended ReaxFF reactive force field. *J. Phys. Chem. A* **114**, 12561–12572 (2010).
50. B. Saha, G. C. Schatz, Carbonization in polyacrylonitrile (PAN) based carbon fibers studied by ReaxFF molecular dynamics simulations. *J. Phys. Chem. B* **116**, 4684–4692 (2012).
51. M. Kowalik, C. Ashraf, B. Damirchi, D. Akbarian, S. Rajabpour, A. C. T. van Duin, Atomistic scale analysis of the carbonization process for C/H/O/N-based polymers with the ReaxFF reactive force field. *J. Phys. Chem. B* **123**, 5357–5367 (2019).
52. P. H. Hermans, *Physics and Chemistry of Cellulose Fibres* (Elsevier, Amsterdam, 1946), pp. 221.
53. L. Martinez, R. Andrade, E. G. Birgin, J. M. Martinez, PACKMOL: A package for building initial configurations for molecular dynamics simulations. *J. Comput. Chem.* **30**, 2157–2164 (2009).
54. H. Sun, COMPASS: An ab initio force-field optimized for condensed-phase applications overview with details on alkane and benzene compounds. *J. Phys. Chem. B* **102**, 7338–7364 (1998).
55. S. Plimpton, Fast parallel algorithms for short-range molecular dynamics. *J. Comput. Phys.* **117**, 1–19 (1995).
56. F. Liu, N. Hu, H. Ning, Y. Liu, Y. Li, L. Wu, Molecular dynamics simulation on interfacial mechanical properties of polymer nanocomposites with wrinkled graphene. *Comput. Mater. Sci.* **108**, 160–167 (2015).
57. T.-Y. Wang, J.-L. Tsai, Investigating thermal conductivities of functionalized graphene and graphene/epoxy nanocomposites. *Comput. Mater. Sci.* **122**, 272–280 (2016).
58. J. R. Gissing, C. Pramanik, B. Newcomb, S. Kumar, H. Heinz, Nanoscale structure–property relationships of polyacrylonitrile/CNT composites as a function of polymer crystallinity and CNT diameter. *ACS Appl. Mater. Interfaces* **10**, 1017–1027 (2018).
59. W. Shinoda, M. Shiga, M. Mikami, Rapid estimation of elastic constants by molecular dynamics simulation under constant stress. *Phys. Rev. B* **69**, 134103 (2004).

**Acknowledgments:** We thank the staff members at the University of Virginia NCMF for electron microscopy technical support, as well as H. Luo from G. M. Geise's group and M. Diasio from D. L. Green's group in Chemical Engineering Department at the University of Virginia for TGA and viscosity test support. We thank X. Xiao (Brookhaven National Laboratory) for performing the tomography experiments. **Funding:** Financial support for this study was provided by the U.S. Department of Energy, Vehicle Technology Office (DE-EE0008195). B.C. is supported by the NSF Graduate Research Fellowship Program under grant no. 1315231. This research used Beamline 18-ID (FXI) of the National Synchrotron Light Source II, a U.S. Department of Energy (DOE) Office of Science User Facility operated for the DOE Office of Science by Brookhaven National Laboratory under contract no. DE-SC0012704. Computational support is provided by the NSF through the extreme science and engineering discovery environment (MSS180008). **Author contributions:** Z.G., L.V.Z., A.C.T.v.D., and X.L. conceived the idea. Z.G. and J.Z. designed and conducted the fiber spinning. Y.S. helped prepare the experiment setup. Z.G. conducted experimental characterization, analysis, and manuscript preparation. Y.S., B.C., and D.B. conducted the nanotomography test. S.R., M.K., and A.C.T.v.D. conducted ReaxFF simulation and analysis. K.J. and L.V.Z. conducted MD simulation and analysis. S.R., K.J., and B.C. helped to co-write the manuscript. C.B., L.Z., K.R.B., Y.S., and J.W.K. helped with the result analysis and manuscript preparation. **Competing interests:** The authors declare that they have no competing interests. **Data and materials availability:** All data needed to evaluate the conclusions in the paper are present in the paper and/or the Supplementary Materials. Additional data related to this paper may be requested from the authors.

Submitted 6 September 2019

Accepted 6 February 2020

Published 24 April 2020

10.1126/sciadv.aaz4191

**Citation:** Z. Gao, J. Zhu, S. Rajabpour, K. Joshi, M. Kowalik, B. Croom, Y. Schwab, L. Zhang, C. Bumgardner, K. R. Brown, D. Burden, J. W. Klett, A. C. T. van Duin, L. V. Zhigilei, X. Li, Graphene reinforced carbon fibers. *Sci. Adv.* **6**, eaaz4191 (2020).

## Graphene reinforced carbon fibers

Zan Gao, Jiadeng Zhu, Siavash Rajabpour, Kaushik Joshi, Malgorzata Kowalik, Brendan Croom, Yosyp Schwab, Liwen Zhang, Clifton Bumgardner, Kenneth R. Brown, Diana Burden, James William Klett, Adri C. T. van Duin, Leonid V. Zhigilei and Xiaodong Li

*Sci Adv* 6 (17), eaaz4191.  
DOI: 10.1126/sciadv.aaz4191

### ARTICLE TOOLS

<http://advances.sciencemag.org/content/6/17/eaaz4191>

### SUPPLEMENTARY MATERIALS

<http://advances.sciencemag.org/content/suppl/2020/04/20/6.17.eaaz4191.DC1>

### REFERENCES

This article cites 57 articles, 0 of which you can access for free  
<http://advances.sciencemag.org/content/6/17/eaaz4191#BIBL>

### PERMISSIONS

<http://www.sciencemag.org/help/reprints-and-permissions>

Use of this article is subject to the [Terms of Service](#)

---

*Science Advances* (ISSN 2375-2548) is published by the American Association for the Advancement of Science, 1200 New York Avenue NW, Washington, DC 20005. The title *Science Advances* is a registered trademark of AAAS.

Copyright © 2020 The Authors, some rights reserved; exclusive licensee American Association for the Advancement of Science. No claim to original U.S. Government Works. Distributed under a Creative Commons Attribution NonCommercial License 4.0 (CC BY-NC).